Monte Carlo simulations of segregation in Pt-Re catalyst nanoparticles

Guofeng Wang [1,*], M A Van Hove [1,2,3], P N Ross [1], and M I Baskes [4]

[1] Materials Sciences Division, Lawrence Berkeley National Laboratory, University of California, Berkeley, CA 94720

[2] Advanced Light Source, Lawrence Berkeley National Laboratory, University of California, Berkeley, CA 94720

[3] Department of Physics, University of California, Davis, CA 95616

[4] MST-8 Structure and Property Relations Group, Los Alamos National Laboratory, Los Alamos, NM 87545

We have investigated the segregation of Pt atoms to the surfaces of Pt-Re nanoparticles using the Monte Carlo method and Modified Embedded Atom Method potentials that we have developed for Pt-Re alloys. The $Pt_{75}Re_{25}$ nanoparticles (containing from 586 to 4033 atoms) are assumed to have disordered fcc configurations and cubo-octahedral shapes (terminated by {111} and {100} facets), while the $Pt_{50}Re_{50}$ and $Pt_{25}Re_{75}$ nanoparticles (containing from 587 to 4061 atoms) are assumed to have disordered hcp configurations and truncated hexagonal bipyramidal shapes (terminated by {0001} and {10$\bar{1}$1} facets). We predict that due to the segregation process the equilibrium Pt-Re nanoparticles would achieve a core-shell structure, with a Pt-enriched shell surrounding a Pt-deficient core. For fcc cubo-octahedral $Pt_{75}Re_{25}$ nanoparticles, the shells consist of almost 100 at.% of Pt atoms. Even in the shells of hcp truncated hexagonal bipyramidal $Pt_{50}Re_{50}$ nanoparticles, the concentrations of Pt atoms exceed 85 at. % (35 at.% higher than the overall concentration of Pt atoms in these nanoparticles). Most prominently, all Pt atoms will segregate to the surfaces in the hcp truncated hexagonal bipyramidal $Pt_{25}Re_{75}$ nanoparticles containing less than 1000 atoms. We also find that the Pt atoms segregate preferentially to the vertex sites, less to edge sites, and least to facet sites on the shell of Pt-Re nanoparticles.

---

*Corresponding author. Fax: (510) 486-5530; Email: gfwang@lbl.gov

I. INTRODUCTION

Bimetallic mixtures of Platinum (Pt) and Rhenium (Re) on alumina have been widely used in petroleum refining for the production of aromatic hydrocarbons for automotive fuels [1]. Extensive experimental studies on this system (for example, Ref. [2,3]) have aimed at revealing the interaction properties between Pt and Re in catalyst nanoparticles (also called "clusters"). Early work on electro-oxidation of H_2, CO and H_2/CO mixtures with Pt-Re bulk alloy electrodes indicates that Pt-Re catalysts could also be applied as electro-catalysts in lower temperature polymer electrolyte fuel cells (PEFCs) [4]. Because the atomic-scale structure and arrangement of the two metals in the surfaces of bimetallic catalyst nanoparticles are important factors controlling their reactivity and selectivity [5,6], it is of great interest to characterize the structure and composition of the surfaces on Pt-Re catalyst nanoparticles. In particular, Pt is a precious active catalyst with a wide range of applications. For economic reasons, it is highly desirable to arrange the Pt atoms to the outer surfaces, so as to be in contact with reactants. In fact, for Pt-Ni and Pt-Co catalysts the segregation of Pt atoms to the surfaces of poly-crystals [7] and nanoparticles [8] has indeed enhanced their catalytic performance in oxygen reduction reactions.

Some experimental techniques provide useful information about catalyst nanoparticles. For example, core-shell structures during nucleation and growth of Pt-Ru nanoparticles have been successfully probed using extended X-ray absorption fine structure (EXAFS) [9] and electrochemical nuclear magnetic resonance (EC-NMR) [10]. However, no similar studies for Pt-Re nanoparticles have been performed yet, possibly due to the difficulty in distinguishing Pt and Re using these techniques (the atomic number is 78 for Pt and 75 for Re). Besides experiments, atomic simulation has proven to be a powerful method to provide insight into the surface chemistry of bimetallic nanoparticles [11-15]. In this work, we used the Monte Carlo simulation method to investigate the surface segregation and the core-shell structures of Pt-Re nanoparticles. Compared to a previous theoretical study that only calculated segregation profiles of irregular shaped Pt-Re particles [14], our atomic-level work investigates the equilibrium shapes and structures of Pt-Re nanoparticles.

The Pt-Re nanoparticles that we are interested in contain up to several thousands of atoms. With such a large system size, accurate first principles methods are impractical for simulating surface segregation in these nanoparticles. Alternatively, the embedded-atom method (EAM) [16,17], which is based on density-functional theory, renders a good description of many-body atomic interactions in metals. One challenge in this work is that the interatomic potentials should be applicable both to Pt, which favors the face-centered cubic (fcc) bulk structure, and to Re, which favors the hexagonal closed packed (hcp) bulk structure. Baskes [18,19] solved this problem by adding directional bonding to EAM thus developing the modified embedded-atom method (MEAM) for metals with various lattices. Therefore, we employed MEAM potentials for Pt and Re in this work. We used first-principles calculation results for Pt-Re intermetallic compounds to determine the cross potential between Pt and Re. Our MEAM potentials (parameters given in Sec. III) should be universal and useful for simulating Pt-Re alloys in other applications.

This paper is structured as follows: in Sec. II we describe the MEAM potentials and Monte Carlo method; in Sec. III we develop MEAM potentials for Pt-Re alloys and apply these potentials to assess surface segregation for extended low-index surfaces; in Sec. IV we report in detail surface segregation in fcc cubo-octahedral $Pt_{75}Re_{25}$ nanoparticles, hcp truncated hexagonal bipyramidal $Pt_{25}Re_{75}$ nanoparticles, and hcp truncated hexagonal bipyramidal $Pt_{50}Re_{50}$ nanoparticles; finally, conclusions are drawn in Sec. VI.

II. SIMULATION METHODS

A. Modified embedded atom method (MEAM)

The detailed description of the MEAM formalism applied to cubic and hcp metals has been documented in the literature [18,19]. Hence, we only give a brief description below.

Within the MEAM, the total energy of a system is calculated as

$$E = \sum_i \left[F(\overline{r}_i) + \frac{1}{2} \sum_{j(\neq i)} \Phi(R_{ij}) \right] \tag{1}$$

In the above equation, $\overline{r}_i$ is the background electron density at the center of atom i obtained by the superposition of electronic densities from its surrounding atoms. The first term is the embedding energy for atom i which is embedded into the electron density $\overline{r}_i$, and the second term is the core-core pair repulsion between atom i and j separated by a distance R_{ij}.

The embedding energy is given as follows:

$$F(\overline{r}) = A E_c (\frac{\overline{r}}{\overline{r}^0}) \ln(\frac{\overline{r}}{\overline{r}^0}) \tag{2}$$

Here, A is an adjustable parameter, E_c is the cohesive energy, and $\overline{r}^0$ is the density scaling parameter.

The electron density $\overline{r}_i$ is composed of the spherically symmetric partial electron density $r_i^{(0)}$ and the angular contributions $r_i^{(1)}$, $r_i^{(2)}$ and $r_i^{(3)}$. These partial electron densities have the following forms:

$$r_i^{(0)} = \sum_{j(\neq i)} r_j^{a(0)}(R_{ij}) \tag{3a}$$

$$\left(r_i^{(1)}\right)^2 = \sum_{a}\left[\sum_{j(\neq i)} x_{ij}^a r_j^{a(1)}(R_{ij})\right]^2 \tag{3b}$$

$$\left(r_i^{(2)}\right)^2 = \sum_{a,b}\left[\sum_{j(\neq i)} x_{ij}^a x_{ij}^b r_j^{a(2)}(R_{ij})\right]^2 - \frac{1}{3}\left[\sum_{j(\neq i)} r_j^{a(2)}(R_{ij})\right]^2 \tag{3c}$$

$$\left(r_i^{(3)}\right)^2 = \sum_{a,b,g}\left[\sum_{j(\neq i)} x_{ij}^a x_{ij}^b x_{ij}^g r_j^{a(3)}(R_{ij})\right]^2 - \frac{3}{5}\sum_{a}\left[\sum_{j(\neq i)} x_{ij}^a r_j^{a(3)}(R_{ij})\right]^2 \tag{3d}$$

Here, $x_{ij}^a = R_{ij}^a / R_{ij}$, and R_{ij}^a is the α component (α = x, y, or z) of the distance vector between atom i and j. $r_j^{a(h)}(R_{ij}) = e^{-b^{(h)}(R_{ij}/r_e - 1)}$ (h=0, 1, 2, and 3) represents the atomic electron densities contributed from atom j to atom i, $\beta^{(h)}$ are adjustable parameters, and r_e is the nearest-neighbor distance in the equilibrium reference structure. Note that Eq. (3d) is different from that in earlier work (for example, Ref. [18,19]). This new modification makes the partial electron densities orthogonal [20]. In this work, we use the following

scheme (see other schemes in Ref. [21]) to combine the partial electron densities and compute the background electron density:

$$\bar{r}_i = r_i^{(0)} \sqrt{1 + \Gamma_i} \tag{4a}$$

$$\Gamma_i = \sum_{h=1}^{3} t^{(h)} \left[r_i^{(h)} / r_i^{(0)} \right]^2 \tag{4b}$$

where $t^{(h)}$ are adjustable parameters.

The pair potential between two atoms separated by a distance R is given by:

$$\Phi(R) = \frac{2}{Z} \left[E^u(R) - F(\bar{r}^0(R)) \right] \tag{5}$$

where Z is the number of nearest neighbors in the bulk reference structure (Z=12 for fcc and hcp metals). $E^u(R)$ is the energy per atom of the reference structure as a function of nearest-neighbor distance R and is determined using the following universal equation of state of Rose et al. [22].

$$E^u(R) = -E_c(1 + a^*)e^{-a^*} \tag{6a}$$

$$a^* = a(R / r_e - 1) \tag{6b}$$

$$a = \sqrt{\frac{9\Omega B}{E_c}} \tag{6c}$$

Here, E_c, r_e, Ω, and B are the cohesive energy, nearest-neighbor distance, atomic volume, and bulk modulus for the equilibrium reference structure, respectively.

$\bar{r}^0(R)$ in Eq. (5) is the background electron density for the reference structure. For fcc metals,

$$\bar{r}^0(R) = Zr^{a(0)}(R) \tag{7a}$$

For hcp metals,

$$\bar{r}^0(R) = Zr^{a(0)}(R) \sqrt{1 + \frac{t^{(3)}}{3Z^2} \left(\frac{r^{a(3)}}{r^{a(0)}} \right)^2} \tag{7b}$$

B. Screening procedure

The current version of the MEAM considers only nearest-neighbor interactions, therefore, we must provide a screening procedure to define which are the nearest

neighbors of an atom. We use the many-body screening function proposed by Baskes [21] using the elliptical construction.

The screening function S_{ik} between atom i and atom k depends on all the other atoms between them, thus

$$S_{ik} = \prod_{j \neq i,k} S_{ijk} \qquad (8a)$$

$$S_{ijk} = f_c(\frac{C - C_{min}}{C_{max} - C_{min}}) \qquad (8b)$$

where $f_c(x)$ is a function of the material dependent parameters C_{max} and C_{min}. The parameter C is determined using the following equation.

$$C = \frac{2(X_{ij} + X_{jk}) - (X_{ij} - X_{jk})^2 - 1}{1 - (X_{ij} - X_{jk})^2} \qquad (9)$$

where $X_{ij} = (r_{ij}/r_{ik})^2$ and $X_{jk} = (r_{jk}/r_{ik})^2$. The r_{ij}, r_{jk}, and r_{ik} are the distances between the corresponding atoms.

The smooth cutoff function $f_c(x)$ in Eq. (8b) assumes the following form.

If $x \geq 1$, $\quad f_c(x) = 1$ $\qquad (10a)$

If $0 < x < 1$, $f_c(x) = \left[1 - (1 - x)^4\right]^2$ $\qquad (10b)$

If $x \leq 0$, $\quad f_c(x) = 0$ $\qquad (10c)$

We multiply the atomic electron density and the pair potentials by the screening function S_{ik}, hence $S_{ik}=1$ represents unscreened interaction while $S_{ik}=0$ represents a completely screened interaction.

C. Monte Carlo method

Monte Carlo (MC) simulation methods based on the Metropolis algorithm [23] have been successfully used in previous surface segregation calculations for various alloys (for example, Pt-Ni [24], Ni-Cu [25], and Al-Mg [26]). These MC methods are particularly advantageous in studying segregation phenomena in the equilibrium alloy structure, because they can circumvent slow physical dynamic processes (such as

diffusion) in the system and provide an averaged composition profile over a thermodynamic equilibrium ensemble [27].

In our calculations, we used statistical mechanics with a canonical ensemble, where the total number of atoms of each element and the temperature are constants. In this approach, starting from some atomic configuration, the successive configurations are generated in proportion to the probabilities of a configuration occurring in the equilibrium ensemble. In each step, one of the following two configuration transformations is tried out with an equal probability:

(1) A randomly selected atom is displaced from its original position in a random direction. The magnitude of the displacement is in the range of $(0, r_{max}]$. At a given temperature, the maximum displacement r_{max} is tuned so that the acceptance rate of new configurations is about 0.5 during the equilibrated part of the simulations.

(2) Two randomly selected atoms with different element types are exchanged.

The operation (1) accounts for the relaxation and vibration processes, and the operation (2) accounts for the inter-diffusion process in the model system.

According to the Boltzmann distribution, the probability (P_{XY}) of the configuration transformation (from X to Y) is given by a Boltzmann factor for the change in energy ($\Delta E = E_Y - E_X$).

$$P_{XY} = \exp(-\frac{\Delta E}{k_B T}) \tag{11}$$

Here, k_B is the Boltzmann constant and T is the temperature. If $P_{XY} \geq 1$ (decrease in energy), the new configuration is always retained, while if $P_{XY} < 1$ (increase in energy), the new configuration is accepted with the probability P_{XY}.

After repeating the above procedures for multi-million MC steps, the physical quantities such as the composition profile are obtained by averaging over the resulting configurations. For example, we used the above Monte Carlo scheme to determine the lattice constants for disordered fcc $Pt_{75}Re_{25}$ and hcp $Pt_{25}Re_{75}$ bulk alloys. To this end, we carried out MC simulations for disordered fcc $Pt_{75}Re_{25}$ and hcp $Pt_{25}Re_{75}$ bulk alloys with various lattice parameters and determined the lattice constant that led to the zero average

pressure (strain) for a 3D periodic simulation cell at a given temperature. In this work, we simulated the disordered fcc $Pt_{75}Re_{25}$ bulk alloy using a cubic simulation cell containing 500 atoms and the hcp $Pt_{25}Re_{75}$ bulk alloy using a hexagonal simulation cell containing 512 atoms. The whole MC simulation typically takes 5 million steps, but we only average the pressure of simulation cells over the last 3 million steps to eliminate the influence of the original structure. For the fcc $Pt_{75}Re_{25}$ bulk alloy the equilibrium lattice constants are found to be a=3.902 Å at 600K and a=3.906 Å at 900 K. For the hcp $Pt_{25}Re_{75}$ bulk alloy the equilibrium lattice constants are a=2.761 Å, c=4.453 Å at 600K and a=2.766 Å, c=4.463 Å at 900 K. The calculated lattice constants are close to a=3.895 Å for the fcc $Pt_{75}Re_{25}$ bulk alloy and a=2.762 Å, c=4.408 Å for the hcp $Pt_{25}Re_{75}$ bulk alloy interpolated from experimental data at nearby temperature [28]. These lattice constants are used to initialize the atomic positions for the extended surface (Sec. III.B) and nanoparticle (Sec. IV) simulations.

III. MEAM DESCRIPTION OF Pt-Re

A. Development of the potentials

Similar to previous work [18,19], the MEAM potentials for fcc Pt and hcp Re were developed using empirical data for the cohesive energy, the lattice constants, the elastic constants, and the vacancy formation energy. These potentials yield a cohesive energy of a Pt atom in the fcc lattice that is 0.022 eV lower than in the hcp lattice (compared to the experimental difference of 0.03 eV [29]), and yield a cohesive energy of a Re atom in the hcp lattice that is 0.084 eV lower than in the fcc lattice (compared to the experimental difference of 0.11 eV [29]).

To determine the cross potentials between Pt and Re, we chose Pt_3Re, which has the $L1_2$ structure, as the reference structure. Hence, the Pt-Re pair potential is evaluated using the following expression [30].

$$\Phi_{Pt\,Re}(R) = \frac{1}{3}E^u_{Pt_3Re}(R) - \frac{1}{4}F_{Pt}(\overline{r}_{Pt}) - \frac{1}{12}F_{Re}(\overline{r}_{Re}) - \Phi_{PtPt}(R) \qquad (12a)$$

where

$$\overline{r}_{Pt} = \sqrt{\left[8r^{a(0)}_{Pt}(R) + 4r^{a(0)}_{Re}(R)\right]^2 + \frac{8}{3}t^{(2)}_{Pt}\left[r^{a(2)}_{Pt}(R) - r^{a(2)}_{Re}(R)\right]^2} \qquad (12b)$$

8

$$\overline{\boldsymbol{r}}_{\mathrm{Re}} = 12\boldsymbol{r}_{P_t}^{a\,(0)}(R) \tag{12c}$$

The parameters for the Pt-Re MEAM potentials are given in Table I, and Table II gives the angular screening parameters for the potentials.

We fit the MEAM cross potentials between Pt and Re with first-principles calculation results of (1) the three elastic constants for Pt_3Re ($L1_2$) and (2) the lattice parameters and cohesive energies for both Pt_3Re ($L1_2$) and $PtRe_3$ ($L1_2$). The cohesive energy for Pt_3Re ($L1_2$) or $PtRe_3$ ($L1_2$) is the energy of these compound crystals relative to the atomic energies of the fcc Pt and the hcp Re. To obtain the above quantum calculation results, we evaluated the energies using density-functional theory (DFT) with the local-density approximation (LDA). We employed the PARATEC code [31]: it is a massively parallel package performing *ab initio* quantum-mechanical total energy calculations using pseudopotentials and a plane-wave basis set. In this work, we used the package FHI98PP [32] to generate the norm-conserving Troullier-Martins [33] type of pseudopotentials, employing common parametrization of the local-density approximation for exchange and correlation. In all calculations, we have used a 16x16x16 k-point grid for k-space integration and a kinetic energy cutoff of 60 Ry to expand the electronic wave-functions in the plane wave basis. The elastic constants are determined following the procedure given in Ref. [34].

Table III compares the calculated properties for Pt_3Re ($L1_2$) and $PtRe_3$ ($L1_2$), showing a generally good agreement between the MEAM potentials and the *ab initio* method except for the cohesive energy of Pt_3Re ($L1_2$). The MEAM predicts the cohesive energy of Pt_3Re ($L1_2$) to be –0.100 eV/atom, while the *ab initio* method gives a value of 0.126 eV/atom. We have tried to develop MEAM potentials to achieve a better agreement for the cohesive energy of Pt_3Re ($L1_2$) between the two methods. However, those potentials do not lead to forming a solid solution for the $Pt_{75}Re_{25}$ alloy at high temperatures, contradicting the experimental Pt-Re phase diagram [35]. In addition, an x-ray investigation for the Pt-Re alloys suggests the existence of a compound with 23 to 25 at.% Re below 1600 °C [36]. Therefore, we developed the MEAM potentials to give the best agreement for the cohesive energy of $PtRe_3$ ($L1_2$) with the *ab initio* calculations.

B. Segregation in extended surfaces

In this section we consider segregation phenomena at surfaces that are infinitely extended in two dimensions. Unlike for nanoparticles, segregation profiles in extended surfaces can currently be measured in experiments. These extended surfaces can then serve as references for the finite-size facets of nanoparticles.

1. Thermodynamics considerations

For randomly disordered binary alloys, surface segregation (the enrichment of one component of the alloy in the surface region relative to bulk composition) can be predicted qualitatively, although not reliably, using the heat of solution of alloys, atom sizes of pure elements, and relative surface energies of pure elements. In the following, we discuss these three properties and their effect on surface segregation for the Pt-Re alloys described with MEAM.

(1) Heat of solution of alloys. The Pt and Re atoms form fcc solid solutions when the Re concentrations $C_{Re} < 40$ at. % and form hcp solid solutions when $C_{Re} > 60$ at. %. For these solid solutions, the heat of solution is negative. Hence, the majority component would be enriched in surfaces. For example, based on this argument the Pt atoms are predicted to segregate to the surfaces of fcc disordered $Pt_{75}Re_{25}$ alloys and Re atoms should enrich in the surfaces of hcp disordered $Pt_{25}Re_{75}$ alloys.

(2) Atom sizes of pure elements. When atom sizes of the two component elements are very different in binary alloys, one or the other element can decrease the atomic mismatch elastic energy by segregating from bulk to surface and it would thus be enriched on surfaces. It is seen in Table IV from the MEAM calculations that pure Pt and pure Re have very similar lattice parameters (i.e. similar atom sizes) in both fcc and hcp crystals. As a result, the elastic energy change would be very small due to surface segregation. Thus, the atom size difference of the pure elements is not an appreciable driving force for surface segregation in Pt-Re alloys.

(3) Relative surface energies of pure elements. The component with a lower surface energy would segregate to the corresponding binary alloy surface. Table IV gives the calculated surface energies of the relaxed low-index fcc and hcp surfaces (shown in

Fig. 1 and Fig. 2) for Pt and Re using our MEAM potentials. For the surfaces of fcc Pt and hcp Re, the calculated surface energies using the MEAM potentials agree quite well with the *ab initio* calculations [37][density-functional theory (DFT) with the generalized gradient approximation (GGA)] and experiments [38, 39]. For both fcc and hcp phases, Pt has significantly lower surface energies than Re. Therefore, Pt atoms would segregate to surfaces in both fcc and hcp Pt-Re disordered alloys considering the relative surface energy difference of the two elements.

2. Monte Carlo simulations

To quantitatively calculate segregation profiles at extended surfaces, we performed Monte Carlo simulations for extended slabs with two surfaces using the MEAM potentials. The slabs expose (111), (100) or (110) surfaces for the fcc lattice, and (0001), $(10\bar{1}1)$, $(10\bar{1}0)_A$, or $(10\bar{1}0)_B$ surfaces for the hcp lattice. For alloys like Pt-Re in which the two component elements have very close atom sizes, atomic relaxation would only weakly affect the calculated segregation profile. Since we here only wish to illustrate the relation between segregation of Pt atoms and atomic sites with various coordination numbers, we fixed the atomic positions in the MC simulations. To model extended surfaces, we used slab simulation cells in which periodic boundary conditions are only applied in the two directions parallel to the surface. The simulated slabs are about 30 Å thick.

In this work, we chose to study segregation on extended surfaces of $Pt_{75}Re_{25}$ alloys (fcc structure) and $Pt_{25}Re_{75}$ alloys (hcp structure). The simulation cells assume the lattice constants determined for the bulk alloys at the same composition and temperature T=900 K (see details in Sec. II.C). The Pt and Re atoms were initially distributed randomly in the whole slab. For each extended surface, we carried out MC simulation for 5 million steps at T=900 K. To eliminate the influence of the initial configurations, we discarded the first 2 million MC steps and sampled the composition profile every 1000 steps in the last 3 million MC steps. To gauge the convergence of our simulations, we compared the calculated compositions for each layer averaged in the two intervals between 2.0-3.5 and 3.5-5.0 million MC steps: we found the difference between the two results to be less than 1 at.%. Because our extended surfaces are modeled as slabs of

finite thickness, the surface segregation alters the composition in the center of the slab; hence, to reestablish the bulk composition there, we have done a series of MC simulations for each extended surface with different overall compositions. We report in Table V and Table VI the segregation profiles from those simulations that lead to the desired bulk compositions (75 at.% Pt for fcc $Pt_{75}Re_{25}$ alloys and 25 at.% Pt for hcp $Pt_{25}Re_{75}$ alloys) in the center of the slabs.

Our simulations show strong segregation of the Pt atoms to both fcc and hcp surfaces. Pt reaches its bulk concentration of fcc $Pt_{75}Re_{25}$ alloys in the second layer for the (111) surface, the third layer for (100), and the fourth layer for (110). For hcp $Pt_{25}Re_{75}$ alloys Pt reaches the bulk concentration in the fourth layer of (0001) and the seventh layer of the other three surfaces [$(10\bar{1}1)$, $(10\bar{1}0)_A$, and $(10\bar{1}0)_B$]. In the outermost layer of the three fcc surfaces of $Pt_{75}Re_{25}$ alloys, the concentration of Pt atoms can achieve 100 at. %. Thus, a pure Pt "skin" could be formed on these surfaces. Surface segregation phenomena are more prominent in the hcp surfaces of $Pt_{25}Re_{75}$ alloys: the concentration difference between the outermost layer and the bulk is at least 66 at.%. On $(10\bar{1}1)$, $(10\bar{1}0)_A$, and $(10\bar{1}0)_B$ surfaces, a pure Pt "skin" can also be formed. We believe that the strong surface segregation for Pt-Re alloys is due to the large surface energy difference (listed in Table V and Table VI) between the two components.

Moreover, our results indicate that the degree of Pt segregation to various surfaces varies, especially to the second layer of those surfaces. Taking the example of the fcc $Pt_{75}Re_{25}$ alloy surfaces, we show in Table V that the Pt atoms segregate strongly to the second layer of (110), segregate slightly to the second layer of (100), and do not segregate to the second layer of (111). It is also seen in Table V that the surface energy differences between pure Pt and Re for various surfaces could not account for the degree of surface segregation. In fact, the number of nearest neighbors (also called coordination number) of atoms on surfaces correlates well with this trend of surface segregation. The atoms in the outermost layer of (110) have only 7 nearest neighbors, while the coordination numbers are 8 for atoms in the outermost layer of (100) and 9 for atoms in the outermost layer of (111). Hence, it appears that Pt atoms segregate preferably to the more "open" surfaces, where surface atoms have fewer nearest neighbors. The surface

segregation results in Table VI for hcp $Pt_{25}Re_{75}$ alloys also support the above correlation between the atomic coordination number and the degree of segregation of Pt atoms. In the outermost layer of (0001), $(10\bar{1}1)$, $(10\bar{1}0)_A$, and $(10\bar{1}0)_B$, the atomic coordination numbers are 9, 8, 8 and 6, respectively. As a result, the Pt atoms segregate more to the more "open" $(10\bar{1}1)$, $(10\bar{1}0)_A$, and $(10\bar{1}0)_B$ surfaces than to the (0001) surfaces. In the second layer of (0001), $(10\bar{1}1)$, $(10\bar{1}0)_A$, and $(10\bar{1}0)_B$, the atomic coordination numbers are 12, 9, 10 and 10, respectively. Correspondingly, the Pt atoms segregate strongly to the second layer of $(10\bar{1}1)$, less strongly to the second layer of $(10\bar{1}0)_A$, and $(10\bar{1}0)_B$, but do not segregate to the second layer of (0001). Therefore, we conclude that *for Pt-Re alloys the Pt atoms would preferentially segregate to atomic positions with fewer nearest neighbors*. Also, it is worth pointing out that the surface energy difference of pure Pt and Re is only a qualitative indicator of which element segregates to surfaces but is not quantitatively related to the magnitude of segregation.

IV. SEGREGATION IN Pt-Re NANOPARTICLES

A. Overview

At a given temperature, segregation profiles for extended surfaces are determined by the composition of alloys. In contrast, segregation in bimetallic nanoparticles is determined by both the composition and the size of the nanoparticle. In the case that one type of atoms in bimetallic nanoparticles segregates strongly to the surface, a core-shell structure is formed. We here start by providing a very simple geometric picture of such a core-shell structure in nanoparticles, governed purely by the surface-to-volume-ratio and the overall composition: this will then serve as a reference when we add the atomic interactions for Pt-Re nanoparticles through MC simulations. Let's assume an infinite tendency of segregation of atoms (thus, one type of atoms will segregate to the surface if a surface site is available). Then we can derive the following equations governing the composition in the core (denoted Cc) and shell (denoted Cs) as a function of overall composition and size (represented by dispersion) of the nanoparticles. In these equations, C stands for overall composition in atomic fraction of the surface-segregating element and D stands for dispersion that is the ratio of the number of surface atoms over the

number of all atoms. The dispersion D is roughly proportional to $N^{-1/3}$, where N is the number of atoms in the nanoparticle.

When C>D, there are more surface-segregating atoms than surface positions in the nanoparticles. Hence, a pure shell of the surface-segregating element is formed, with a mixed core:

$$C_s = 1 \qquad\qquad\qquad\qquad (13a)$$

$$C_c = \frac{C - D}{1 - D} \qquad\qquad\qquad\qquad (13b)$$

When C<D, there are more surface positions than surface-segregating atoms in the nanoparticles. Hence, a pure core of the non-surface-segregating element is formed, with a mixed shell:

$$C_s = \frac{C}{D} \qquad\qquad\qquad\qquad (14a)$$

$$C_c = 0 \qquad\qquad\qquad\qquad (14b)$$

Note that when C=D, C_s=1 and C_c=0: the shell and core are both pure.

Figure 3 plots this geometric argument schematically as a simple phase diagram of core-shell structures, showing both composition and dispersion governing equilibrium configurations of bimetallic nanoparticles. This plot indicates: (1) for a fixed composition C, nanoparticles can change from pure-shell configurations to pure-core configurations with increasing dispersion D (i.e. decreasing size); and (2) for a given dispersion D (i.e. particle size), nanoparticles can change from pure-shell configurations to pure-core configurations with decreasing composition C.

We now address nanoparticles composed of Pt and Re. Pt atoms will presumably segregate strongly to surfaces of Pt-Re nanoparticles based on our results in Sec. III.B.2 for extended surfaces. However, the segregation tendency of Pt atoms to surfaces is not infinitely large at non-zero temperatures. It is anticipated that Eq. (13) or Eq. (14) are applicable to Pt-Re nanoparticles only when C is much smaller or larger than D, respectively. When C is comparable to D, the core-shell structure will deviate from either Eq. (13) or Eq. (14): neither shell nor core will be pure. Therefore, in our MC studies, we investigated segregation in Pt-Re nanoparticles with four different sizes (dispersion

ranges from 0.25 to 0.50) and with three compositions: $Pt_{75}Re_{25}$ (C>>D regime), $Pt_{25}Re_{75}$ (C<<D regime), and $Pt_{50}Re_{50}$ (C≈D regime).

For each nanoparticle, we performed MC simulations allowing both atomic displacement and exchange of element types for 20 million MC steps at T=600 K. The Pt-Re nanoparticles initially had the lattice constants determined for the bulk alloys at the same composition and temperature 600 K (see details in Sec. II.C) with randomly distributed Pt and Re atoms. During the MC simulations, both the lattice constants and the distribution of Pt and Re atoms in the nanoparticles change. The reported concentrations of Pt atoms in the remainder of this section are the averaged values sampled every 10000 MC steps in the last 10 million MC steps.

B. Segregation in $Pt_{75}Re_{25}$ and $Pt_{25}Re_{75}$ nanoparticles

Referring to the Pt-Re phase diagram [35], we assumed the fcc cubo-octahedral shape (terminated by {111} and {100} facets, shown in Fig. 4) for $Pt_{75}Re_{25}$ nanoparticles and the hcp truncated hexagonal bipyramidal shape (terminated by {0001} and {$10\overline{1}1$} facets, shown in Fig. 5) for $Pt_{25}Re_{75}$ nanoparticles. These two shapes are believed to be the equilibrium shapes for fcc and hcp nanoparticles from the macroscopic view of single crystal surface energy [40]. To study the size effect on segregation in nanoparticles, we chose sequences of "magic" numbers of atoms (i.e., nanoparticles containing complete shells of atoms): 586, 1289, 2406, and 4033 for fcc cubo-octahedral nanoparticles, and 587, 967, 2157, and 4061 for hcp truncated bipyramidal nanoparticles. The diameter of these nanoparticles ranges from 2.5 to 5 nm. In our MC simulations at T=600 K, we observed no tendency for a qualitative change in the nanoparticle shape away from cubo-octahedron or away from truncated hexagonal bipyramid. However, we notice that both the fcc $Pt_{75}Re_{25}$ nanoparticles and the hcp $Pt_{25}Re_{75}$ nanoparticles are more rounded after relaxation. This requires the vertex atoms to move inward and/or the central facet atoms to move outward. Some more of the important results are presented below.

1. Core-shell structures

Inside fcc and hcp nanoparticles, each atom has twelve nearest neighbors (nn) just like in bulk crystals. In contrast, atoms on the outermost layer of nanoparticles have an

incomplete set of nearest neighbors. Following the approach proposed in Ref. [40] based on the number and arrangement of nearest neighboring atoms, we can distinguish atoms in the surfaces or in the core of nanoparticles, and further distinguish various surface sites: facet, edge, and vertex (see the figure captions of Fig. 4 and 5). In this work, we define the nearest neighbors for each atom in the nanoparticles as those atoms with a screening factor S (Eq. 8(a)) larger than 0.5 when Cmax=2.8 and Cmin=0.0. We make this choice because for each atom in bulk fcc and hcp Pt-Re alloys, the screening factor would be 1.0 between this atom and its 12 nearest neighbors and 0.2 between this atom and its second nearest neighbors if we choose the C's above. Our definition leads to results consistent with direct visualizations.

Figure 6 shows clearly the equilibrium core-shell structures of Pt-Re nanoparticles using cross-sections that expose the centers of the nanoparticles. In both fcc $Pt_{75}Re_{25}$ nanoparticles and hcp $Pt_{25}Re_{75}$ nanoparticles, the Pt is enriched in the shell region and correspondingly depleted in the core region. The core-shell difference of concentration of Pt atoms can be as high as 67.2 at.% for the hcp $Pt_{25}Re_{75}$ nanoparticle containing 2157 atoms. Tables VII and VIII give the calculated concentrations of Pt atoms in the shell and core of the nanoparticles. Table VII shows that the shell of fcc $Pt_{75}Re_{25}$ nanoparticles with number of atoms ranging from 586 to 4033 is composed of almost 100 at.% Pt atoms, agreeing excellently with the prediction from Eq. (13). The agreement between simulations and Eq. (13) is best for the nanoparticle with 4033 atoms, for which C=0.75 is much larger than D=0.274. It is noticeable in Table VIII that the Pt atoms would be almost absent in the core of the hcp $Pt_{25}Re_{75}$ nanoparticles containing fewer than 1000 atoms, although Pt and Re form solid solutions in the bulk materials at the same composition. This agrees with Eq. (14) since C=0.25 is much smaller than D=0.460 and D=0.399. As expected, a much larger discrepancy between simulations and Eq. (13) and Eq. (14) is observed for the nanoparticle containing 4061 atoms, for which D=0.259 is approximately equal to C=0.25.

2. {100}-facet reconstruction in fcc $Pt_{75}Re_{25}$ nanoparticles

We found that a reconstruction process often occurs after many simulation steps in {100} facets of fcc $Pt_{75}Re_{25}$ nanoparticles: Figure 7 displays this process. Figure 7(a)

shows the initial configuration of the fcc $Pt_{75}Re_{25}$ nanoparticle containing 586 atoms. At this time, the Pt and Re atoms are distributed randomly and the 4x4 atoms in the (100) facet (marked with dashed lines) are in their bulk positions forming a square. Figure 7(b) shows the same nanoparticle after 5 million MC steps. It can be seen that the Pt atoms have segregated to the surface and form a nearly pure Pt "skin" covering this nanoparticle. Moreover, some of the 4x4 atoms in the (100) facet have moved significantly away from their original positions. It is shown in Fig. 7(c) that some atoms from inside the nanoparticle have moved toward the (100) facet and in Fig. 7(d) that seven atoms (where there were four before) eventually arrange themselves into a denser hexagonal configuration in the top layer of the (100) facet, leaving the external edge of the 4x4 array intact near bulk-like positions, but distorted away from a square shape toward a diamond shape.

To our knowledge, no previous studies have reported this phenomenon in nanoparticles. However, the reconstruction of {100} facets from square to hexagonal lattice in the Pt enriched shell of nanoparticles is reasonable and anticipated. Indeed, it is well known that (100) surfaces of pure elemental Pt undergo a similar surface reconstruction to a hexagonal outermost layer [41,42]. In addition, low energy electron diffraction (LEED) shows that the top layer of the (100) surface of Pt_3Co alloys can reconstruct from a square lattice to a hexagonal lattice if the Pt atoms strongly segregate to the top layer of the surface [43]. Therefore, we conclude from our simulations that *the top layer of the {100} facets in fcc cubo-octahedral $Pt_{75}Re_{25}$ nanoparticles can reconstruct from a square lattice to a denser hexagonal lattice and that the extra atoms needed in this process come from the core of the nanoparticles (not the surrounding edges and vertices).*

3. Preferential segregation in hcp $Pt_{25}Re_{75}$ nanoparticles

For hcp $Pt_{25}Re_{75}$ nanoparticles, our results in Table IX indicate that the segregation of Pt atoms to the outermost layer of nanoparticles is site dependent. The general trend is that Pt atoms preferentially segregate to the surface sites with a lower coordination number, i.e., Pt atoms would segregate most to vertices, less to edges, and least to facets of Pt-Re nanoparticles. This observation agrees with our finding in

17

Sec.III.B.2 for segregation to extended surfaces, namely, that Pt atoms would preferentially segregate to atomic positions with fewer nearest neighbors. These results are also consistent with the previous work [14] for irregularly shaped Pt-Re nanoparticles using Monte Carlo simulations combined with a "macroscopic atom" model.

C. Segregation in $Pt_{50}Re_{50}$ nanoparticles

From the Pt-Re phase diagram [35], it is known that the fcc (Re in Pt) solid solution and hcp (Pt in Re) solid solution co-exist in bulk $Pt_{50}Re_{50}$ alloys at low temperatures (<2737 K). Hence, it is not clear *a priori* which lattice structure (fcc or hcp) the $Pt_{50}Re_{50}$ nanoparticle would assume at 600K. An experimental study in a similar case of Pt-Ru nanoparticles (Ru is a hcp metal) shows that both fcc and hcp nanoparticles could be found at this composition after co-reduction at 673 K [44].

The atomic cohesive energy, which is the total potential energy (U) divided by the number of atoms (N) indicates the relative stability of nanoparticles with different lattices and shapes. Figure 8 shows our calculated atomic cohesive energy as a function of the number of atoms for fcc cubo-octahedral and hcp truncated hexagonal bipyramidal $Pt_{50}Re_{50}$ nanoparticles. For all these nanoparticles (distinguished by lattice and shape) in our study, an approximately linear relation between U/N and $N^{-1/3}$ is observed.

$$\frac{U}{N} \approx E_B + k \cdot N^{-\frac{1}{3}} \tag{13}$$

In the above equation, E_B (<0) is the bulk cohesive energy. The term $kN^{-1/3}$ represents the contribution to the cohesive energy from surface atoms, whose number is approximately proportional to $N^{2/3}$. A similar relation between atomic cohesive energy and number of atoms was found previously for pure metal nanoparticles [45,46].

The upper two lines in Fig. 8 for $Pt_{50}Re_{50}$ nanoparticles, in which Pt and Re atoms are distributed randomly, were obtained by a linear fit to the average atomic cohesive energy for 20 distinct configurations. The lower two lines in Fig. 8 for $Pt_{50}Re_{50}$ nanoparticles, in which Pt atoms segregate to the surfaces, were linear fits to the average atomic cohesive energy from MC simulations (T=600K, without atom displacements, total length of 10 million MC steps and data analysis for the last 8 million MC steps). In both cases assuming the bulk crystal structure, we used a=3.902 Å to determine the initial

atom positions in fcc $Pt_{50}Re_{50}$ nanoparticles, and a=2.761 Å, c=4.453 Å in hcp $Pt_{50}Re_{50}$ nanoparticles.

For $Pt_{50}Re_{50}$ nanoparticles (Pt and Re atoms are distributed randomly) containing the same number of atoms (N), our results in Fig. 8 indicate that the atomic cohesive energy for atoms in fcc and hcp nanoparticles do not differ by much. Compared to the corresponding hcp nanoparticle, the fcc nanoparticle has a lower energy when the particle size is small (for example, 0.007 eV lower when N=500), a higher energy when the particle size is large (for example, 0.007 eV higher when N=5000), and an equal energy when the number of atoms is about N=3273. In contrast, the atomic cohesive energy for atoms in the hcp $Pt_{50}Re_{50}$ nanoparticle is always about 0.02 eV lower than in the corresponding fcc nanoparticle after the Pt atoms segregate to the surface. This implies that the hcp truncated hexagonal bipyramid would be the equilibrium lattice and shape of $Pt_{50}Re_{50}$ nanoparticles considering surface segregation phenomena. This is reasonable because a hcp Re-enriched core would be preferred after almost all Pt atoms segregate to the surface. Experimental studies [47] confirm that the Pt atoms can form a layer, sharing the hcp lattice, on top of the Re crystal. It is noticed that the energy difference 0.02 eV/atom between fcc and hcp nanoparticles is comparable to k_BT =0.05 eV/atom at 600K. Therefore, we anticipate that both fcc and hcp $Pt_{50}Re_{50}$ nanoparticles may coexist at 600 K.

Starting from the hcp truncated hexagonal bipyramidal $Pt_{50}Re_{50}$ nanoparticles with a random distribution of Pt and Re atoms, we carried out Monte Carlo simulations with atomic relaxations up to 20 million MC steps at 600 K. Table X reports the concentration of Pt atoms in the shell and core of the equilibrium hcp $Pt_{50}Re_{50}$ nanoparticles. Compared to the results in Table VIII for the $Pt_{25}Re_{75}$ nanoparticle with the same shape, the concentration of Pt atoms in the shell of the $Pt_{50}Re_{50}$ nanoparticle containing 587 atoms increases by 31.2 at.% (higher than the overall concentration difference 25 at.%). In contrast, the increase of the Pt concentration in the shell of the other three larger $Pt_{50}Re_{50}$ nanoparticles is less than 25 at.%. Nonetheless, a rather higher concentration of Pt atoms (over 85 at.%) on the surface of hcp $Pt_{50}Re_{50}$ nanoparticles can be achieved due to segregation. Not surprisingly, neither Eq. (13) nor Eq. (14) is applicable for accurately

19

predicting core-shell structures of $Pt_{50}Re_{50}$ nanoparticles because C=0.50 is comparable to D ranging from 0.260 to 0.451.

V. CONCLUSIONS

In this work, we investigated the segregation of Pt atoms to surfaces of bimetallic Pt-Re nanoparticles. To this end, we first developed MEAM potentials for the Pt-Re alloys based on experimental and first principles calculation results. Our MEAM potentials can reproduce most of the available results for the elemental Pt, elemental Re and intermetallic Pt-Re compounds. More importantly, these potentials lead to correct surface energies for Pt and Re. The surface energy emerges as a major factor controlling the segregation of Pt atoms in Pt-Re bulk alloy surfaces and nanoparticles.

From the study of Pt-Re surfaces [(111), (100), and (110) for fcc $Pt_{75}Re_{25}$ alloys and (0001), (10$\overline{1}$1), (10$\overline{1}$0)$_A$, and (10$\overline{1}$0)$_B$ for hcp $Pt_{25}Re_{75}$ alloys], we find that the Pt atoms always segregate to the surfaces. Furthermore, we find that the Pt atoms would preferentially segregate to those sites that have lower coordination number. We also confirmed this conclusion in the simulations for Pt-Re nanoparticles. These results imply that the concentrations of Pt atoms at various sites in Pt-Re nanoparticles are predicted to increase with lowering coordination number in the order from particle core to facets, edges, and vertices.

We assume the fcc cubo-octahedron and hcp truncated hexagonal bipyramid to be the equilibrium shapes for $Pt_{75}Re_{25}$ and $Pt_{25}Re_{25}$ nanoparticles, respectively. One interesting observation is that the {100} facets in fcc cubo-octahedral $Pt_{75}Re_{25}$ nanoparticles are predicted to reconstruct from the bulk terminated square lattice to a hexagonal arrangement of atoms after a high concentration of Pt atoms is achieved due to segregation. The extra atoms for the hexagonal lattice come from the core region, not from the surrounding edges or vertices. Furthermore, we investigated the equilibrium shapes and core-shell structures for $Pt_{50}Re_{50}$ nanoparticles. We find that both the fcc cubo-octahedral and hcp truncated hexagonal bipyramidal $Pt_{50}Re_{50}$ nanoparticles are thermodynamically stable, although the segregation of the Pt atoms to their surface makes the hcp truncated hexagonal bipyramidal nanoparticles energetically more favorable.

Our results indicate that at T=600 K the equilibrium Pt-Re nanoparticles adopt a core-shell structure: the shell contains a higher concentration of Pt atoms than the core. For fcc cubo-octahedral $Pt_{75}Re_{25}$ nanoparticles, the shells consist of almost 100 at.% Pt atoms due to segregation, achieving a nearly pure Pt-shell structure. In the shells of hcp truncated hexagonal bipyramidal $Pt_{50}Re_{50}$ nanoparticles, the concentration of Pt atoms exceeds 85 at. %. All Pt atoms are predicted to segregate to the surfaces (mostly to vertices, less to edges, and least to facets) of the hcp truncated hexagonal bipyramidal $Pt_{25}Re_{75}$ nanoparticles containing less than 1000 atoms, leading to a pure Re-core structure, as qualitatively predicted with Eq. (14). The core-shell structure of Pt-Re nanoparticles revealed in this work should be useful for the future processing, improvement, and design of Pt-Re catalyst nanoparticles.

ACKNOWLEDGMENTS

References:

[1] J.H. Sinfelt, *Bimetallic Catalysts: Discoveries, concepts, and Applications*, (Wiley, New York, 1983).

[2] K.S. Liang, F.Z. Chien, G.J. Hughes, G.D. Meitzner, and J.H. Sinfelt, J. Phys. Chem. **95**, 9974 (1991).

[3] F. Hilbrig, C. Michel, and G.L. Haller, J. Phys. Chem. **96**, 9893 (1992).

[4] B.N. Grgur, N.M. Markovic, and P.N. Ross, Electrochimica Acta. **43**, 3631 (1998).

[5] G.A. Somorjai and Y.G. Borodko, Catal. Lett. **1**, 76 (2001).

[6] J.H. Sinfelt, Rev. Mod. Phys. **51**, 569 (1979).

[7] V. Stamenkovic, T.J. Schmidt, P.N. Ross, and N.M. Markovic, J. Phys. Chem. B **106**, 11970 (2002).

[8] U.A. Paulus, A. Wokaun, G.G. Scherer, T.J. Schmidt, V. Stamenkovic, V. Radmilovic, N.M. Markovic, and P.N. Ross, J. Phys. Chem. B **106**, 4181 (2002).

[9] M.S. Nashner, A.I. Frenkel, D. Somerville, C.W. Hills, J.R. Shapley, and G. Nuzzo, J. Am. Chem. Soc. **120**, 8093 (1998).

[10] P.K. Babu, H.S. Kim, E. Oldfield, and A. Wieckowski, J. Phys. Chem. B **107**, 7595 (2003).

[11] J.K Strohl and T.S. King, J. Catal. **116**, 540 (1989).

[12] D.S. Mainardi and P.B. Baluena, Langmuir **17**, 2047 (2001).

[13] E. Christoffersen, D. Stoltze, and J.K. Nørskov, Surf. Sci. **505**, 200 (2002).

[14] S. Helfensteyn and C. Creemers, Surf. Sci. **507-510**, 783 (2002).

[15] C. Mottet, G. Tréglia, and B. Legrand, Phys. Rev. B **66**, 045413 (2002).

[16] M.S. Daw and M.I. Baskes, Phys. Rev. Lett. **50**, 1285 (1983).

[17] M.S. Daw and M.I. Baskes, Phys. Rev. B **29**, 6443 (1984).

[18] M.I. Baskes, Phys. Rev. B **62**, 2727 (1992).

[19] M.I. Baskes and R.A. Johnson, Modell. Simul. Mater. Sci. Eng. **2**, 147 (1994).

[20] M.I. Baskes, Mater. Sci. Eng., A **261**, 165 (1999).

[21] M.I. Baskes, Mater. Chem. Phys. **50**, 152 (1997).

[22] J.H. Rose, J.R. Smith, F. Guinea, and J. Ferrante, Phys. Rev. B **29**, 2963 (1984).

[23] N. Metropolis, A.W. Rosenbluth, M.N. Rosenbluth, A.H. Teller, and E. Teller, J. Chem. Phys. **21**, 1087 (1953).

[24] P. Deurinck and C. Creemers, Surf. Sci. **441,** 493 (1999).

[25] S.M. Foiles, Phys. Rev. B **32,** 7685 (1985).

[26] X.Y. Liu, P.P. Ohotnicky, J.B. Adams, C.L. Rohrer, and R.W. Hyland, Surf. Sci. **373,** 357 (1997).

[27] S.M. Foiles, *Surface Segregation Phenomena*, Eds. P.A. Dowben and A. Miller (CRC press, Boca Raton, FL, 1990), p.79.

[28] W.B. Pearson, *A Handbook of Lattice Spacings and Structures of Metals and Alloys*, (Pergamon, Oxford, 1964), p. 894.

[29] N. Saunders, A.P. Miodownik, and A.T. Dinsdale, CALPHAD **12**, (1988) 351.

[30] M.I. Baskes, J.E. Angelo, and C.L. Bisson, Modell. Simul. Mater. Sci. Eng. **2**, 505 (1994).

[31] B.G. Pfrommer, J. Demmel, and H. Simon, J. Comp. Phys. **150**, 287 (1999); B. G. Pfrommer, M. Coté, S. G. Louie, and M. L. Cohen, J. Comp. Phys. **131**, 233 (1997); also see details at website http://www.nersc.gov/projects/paratec.

[32] M. Fuchs and M. Scheffler, Comput. Phys. Commun. **119**, 67 (1999).

[33] N. Troullier and J. L. Martins, Phys. Rev. B **43**, 1993 (1991).

[34] P. Söderlind, O. Eriksson, J.M. Wills, and A.M. Boring, Phys. Rev. B **48**, 5844 (1993).

[35] *Binary Alloy Phase Diagrams*, 2nd ed., Vol. 3, Ed.-in-Chief: TB Massalski (ASM International, Materials Park, OH, 1990), p3121.

[36] L.I. Voronova, V.P. Polyakova, and E.M. Savitskii, Russ. Metall. **1,** 185 (1984).

[37] L. Vitos, A.V. Ruban, H.L. Skriver, and J. Kollár, Surf. Sci. **411**, 186 (1998).

[38] W.R. Tyson and W.A. Miller, Surf. Sci. **62**, 267 (1977).

[39] F.R. de Boer, R.Room, W.C. Mattens, A.R. Miedema, A.K. Niessen, *Cohesion in Metals* (North-Holland, Amsterdam, 1988).

[40] R. Van Hardeveld and F. Hartog, Surf. Sci. **15**, 189 (1969).

[41] M.A. Van Hove, R.J. Koestner, P.C. Stair, J.P. Bibérian, L.L. Kesmodel, I. Bartoš, and G.A. Somorjai, Surf. Sci. **103**, 189 (1981).

[42] M.A. Van Hove, R.J. Koestner, P.C. Stair, J.P. Bibérian, L.L. Kesmodel, I. Bartoš, and G.A. Somorjai, Surf. Sci. **103**, 218 (1981).

[43] U. Bardi, B.C. Beard, and P.N. Ross, J. Catal. **124**, 22 (1990).

[44] C.W. Hills, N.H. Mack, and R.G. Nuzzo, J. Phys. Chem. B **107**, 2626 (2003).

[45] C.L. Cleveland and U. Landman, J. Chem. Phys. **94**, 7376 (1991).

[46] J. Uppenbrink and D.J. Wales, J. Chem. Phys. **96**, 8520 (1992).

[47] D.J. Godbey and G.A. Somorjai, Surf. Sci. **202**, 204 (1988).

TABLE I Parameters for the MEAM potentials of Pt, Re and Pt-Re. The parameters are: the cohesive energy E_c (eV), the equilibrium nearest-neighbor distance r_e (Å), the exponential decay factor for the universal energy function α, the scaling factor for the embedding energy A, the four exponential decay factors for the atomic densities $\beta^{(i)}$, the four weighting factors for the atomic densities $t^{(i)}$, and the density scaling factor ρ^0.

	E_c	r_e	α	A	$\beta^{(0)}$	$\beta^{(1)}$	$\beta^{(2)}$	$\beta^{(3)}$	$t^{(0)}$	$t^{(1)}$	$t^{(2)}$	$t^{(3)}$	ρ^0
Re	8.09	2.75	6.11	1.09	1.65	1.00	3.00	2.00	1.00	7.00	5.00	-8.00	0.40
Pt	5.77	2.77	6.44	1.04	4.673	2.20	6.00	2.20	1.00	4.70	-1.38	3.29	0.44
PtRe	6.45	2.747	6.71	-	-	-	-	-	-	-	-	-	-

TABLE II. Angular screening parameters for the MEAM potentials.

	Pt-Pt-Pt	Pt-Re-Pt	Re-Pt-Pt	Re-Re-Pt	Re-Pt-Re	Re-Re-Re
C_{max}	2.8	2.8	2.8	2.8	2.8	2.8
C_{min}	2.0	2.0	2.0	2.0	2.0	2.0

TABLE III. Comparison of the calculated properties of bulk Pt_3Re ($L1_2$) and $PtRe_3$ ($L1_2$) using the MEAM potentials and the *ab initio* (LDA-DFT) method.

	MEAM	LDA-DFT
Properties of Pt_3Re ($L1_2$)		
Lattice constant (Å)	3.885	3.885
Cohesive energy (eV/atom)	-0.100	0.126
Elastic constant B (GPa)	352.5	351.1
Elastic constant $(C_{11}-C_{22})/2$ (GPa)	82.0	83.4
Elastic constant C_{44} (GPa)	153.2	174.6
Properties of $PtRe_3$ ($L1_2$)		
Lattice constant (Å)	3.874	3.848
Cohesive energy (eV)	-0.067	-0.075

TABLE IV. Energies of the relaxed extended low-index fcc and hcp surfaces (Fig. 1 and Fig. 2) for pure Pt and pure Re calculated using the MEAM potentials. For comparison, we include the *ab initio* and experimental results for fcc Pt and hcp Re. The equilibrium lattice parameters for Pt and Re in different lattices are given in the second column.

	Lattice	Surface	MEAM (mJ/m^2)	*ab initio* [a] (mJ/m^2)	Experiment (mJ/m^2)
Re	hcp	(0001)	3955	4214	3626 [b], 3600 [c]
	a=2.764 Å	(10$\bar{1}$0)$_A$	3809	4628	
	c/a=1.608	(10$\bar{1}$0)$_B$	4343	5985	
		(10$\bar{1}$1)	4156		
Pt	hcp	(0001)	1577		
	a=2.764 Å	(10$\bar{1}$0)$_A$	1756		
	c/a=1.649	(10$\bar{1}$0)$_B$	2183		
		(10$\bar{1}$1)	1887		
Re	fcc	(111)	3786		
	a=3.893 Å	(100)	4174		
		(110)	3678		
Pt	fcc	(111)	1651	2299	2489 [b], 2475 [c]
	a=3.920 Å	(100)	2155	2734	
		(110)	1963	2819	

[a] Reference [37].

[b] Reference [38].

[c] Reference [39].

TABLE V. Calculated segregation profiles in extended surfaces for disordered fcc $Pt_{75}Re_{25}$ alloys at 900K. C_i (i=1,2,3) is the Pt concentration in layer i and in atomic percent. Also listed in the table are the surface energy differences ($E_S^{Pt} - E_S^{Re}$) of pure Pt and Re calculated using the MEAM potentials.

Surface	C_1	C_2	C_3	$E_S^{Pt} - E_S^{Re}$ (mJ/m^2)
(111)	100	74	75	-2135
(100)	100	79	74	-2019
(110)	100	91	64	-1715

TABLE VI. Calculated segregation profiles in extended surfaces for disordered hcp $Pt_{25}Re_{75}$ alloys at 900K. C_i (i=1,2,3) is the Pt concentration in layer i and in atomic percent. Also listed in the table are the surface energy differences ($E_S^{Pt} - E_S^{Re}$) of pure Pt and Re calculated using the MEAM potentials.

Surface	C_1	C_2	C_3	$E_S^{Pt} - E_S^{Re}$ (mJ/m^2)
(0001)	93	15	29	-2378
($10\bar{1}1$)	99	89	16	-2269
($10\bar{1}0$)$_A$	100	50	14	-2053
($10\bar{1}0$)$_B$	100	53	14	-2160

TABLE VII. Dispersion (D) and concentrations of Pt atoms in atomic percent in the shell (denoted C_s) and core (denoted C_c) of fcc cubo-octahedral $Pt_{75}Re_{25}$ nanoparticles containing different number of atoms (N). Also included is the calculated C_c using Eq. 13(b).

N	D	C_s	C_c	C_c (Eq. 13(b))
586	0.483	96.7	54.9	51.6
1289	0.388	97.7	60.6	59.2
2406	0.325	98.8	63.6	63.0
4033	0.274	99.1	65.9	65.6

TABLE VIII. Dispersion (D) and concentrations of Pt atoms in atomic percent in the shell (denoted C_s) and core (denoted C_c) of hcp truncated bipyramidal $Pt_{25}Re_{75}$ nanoparticles containing different number of atoms (N). Also included is the calculated C_s using Eq. 14(a).

N	D	C_s	C_c	C_s (Eq. 14(a))
587	0.460	54.3	0.2	54.3
967	0.399	62.0	0.5	62.7
2157	0.313	71.2	4.0	79.9
4061	0.259	72.9	8.3	96.5

TABLE IX. Concentrations of Pt atoms (in atomic percent) at various atomic sites [distinguished by the number and arrangement of nearest neighbors (nn)] in the outermost surface of hcp truncated bipyramidal $Pt_{25}Re_{75}$ nanoparticles for a series of particle sizes, with N = number of atoms. Figure 5 shows the positions of various atomic sites (numbered in the same sequence) in nanoparticles.

Atomic sites	N=587	N=967	N=2157	N=4061
1: vertex (5nn)	79	98	100	100
2: vertex (6nn)	97	100	100	100
3: $\{10\bar{1}1\}/\{10\bar{1}1\}$ edges (6nn)	82	85	93	95
4: $\{10\bar{1}1\}/\{10\bar{1}1\}$ edges (7nn)	69	85	92	95
5: $\{10\bar{1}1\}/\{0001\}$ edges (7nn)	63	55	94	95
6: $\{10\bar{1}1\}/\{0001\}$ edges (7nn)	82	82	99	99
7: $\{10\bar{1}1\}/\{10\bar{1}1\}$ edges (8nn)	60	67	86	91
8: $\{10\bar{1}1\}$ facets (8nn)	46	63	77	79
9: $\{0001\}$ facets (9nn)	56	66	66	69
10: $\{10\bar{1}1\}$ facets (9nn)	35	40	50	55

TABLE X. Dispersion (D) and concentrations of Pt atoms in atomic percent in the shell (denoted C_s) and core (denoted C_c) of hcp truncated bipyramidal $Pt_{50}Re_{50}$ nanoparticles containing different number of atoms (N).

N	D	C_s	C_c
587	0.451	85.5	21.0
967	0.395	84.8	27.4
2157	0.315	86.0	33.5
4061	0.260	86.5	37.2

Figure Captions:

FIG. 1. Side views (upper panels) and top views (lower panels) of the extended low-index fcc surfaces: (a) (111), (b) (100), and (c) (110). For illustration, the atoms in the second layer of these surfaces are drawn in gray. The atoms in the outermost layer of (111) surfaces have 9 nearest neighbors; the atoms in the outermost layer of (100) surfaces have 8 nearest neighbors; and the atoms in the outermost layer of (110) surfaces have 7 nearest neighbors. All the other atoms have the complete set of 12 nearest neighbors, as in bulk fcc crystals.

FIG. 2. Side views (upper panels) and top views (lower panels) of the extended low-index hcp surfaces: (a) (0001), (b) $(10\bar{1}1)$, (c) $(10\bar{1}0)_A$ and (d) $(10\bar{1}0)_B$. For illustration, the atoms in the second layer of these surfaces are drawn in gray. The atoms in the outermost layer of (0001) surfaces have 9 nearest neighbors (nn); the atoms in the outermost and second layers of $(10\bar{1}1)$ surfaces have 8 nn and 9 nn, respectively; the atoms in the outermost and second layers of $(10\bar{1}0)_A$ surfaces have 8nn and 10nn, respectively; and the atoms in the outermost and second layers of $(10\bar{1}0)_B$ surfaces have 6nn and 10nn, respectively. All the other atoms have the complete set of 12 nearest neighbors, as in bulk hcp crystals.

FIG. 3. A simple phase diagram of bimetallic nanoparticle core-shell structure with composition C and dispersion D. In the insets, the white circles stand for atoms of the segregating element and the gray background represents the atoms of the other element.

FIG. 4. A fcc cubo-octahedral nanoparticle. The numbers indicate the surface sites on the outermost layer of the particles. The surface atoms at different surface sites have different numbers of nearest neighbors (nn): atom 1: vertex (6nn); atom 2: {111}/{111} edge (7nn); atom 3: {111}/{110} edge (7nn); atom 4: {100} facet (8nn); and atom 5: {111} facet (9nn).

FIG. 5. A hcp truncated hexagonal bipyramidal nanoparticle. The numbers indicate the surface sites on the outermost layer of the particles. The surface atoms at different surface sites have different numbers of nearest neighbors (nn): atom 1: vertex

(5nn); atom 2: vertex (6nn); atom 3: $\{10\bar{1}1\}/\{10\bar{1}1\}$ edge (6nn); atom 4: $\{10\bar{1}1\}/\{10\bar{1}1\}$ edge (7nn); atom 5: $\{10\bar{1}1\}/\{0001\}$ edge (7nn); atom 6: $\{10\bar{1}1\}/\{0001\}$ edge (7nn); atom 7: $\{10\bar{1}1\}/\{10\bar{1}1\}$ edge (8nn); atom 8: $\{10\bar{1}1\}$ facet (8nn); atom 9: $\{0001\}$ facet (9nn); and atom 10: $\{10\bar{1}1\}$ facet (9nn). Note: Although atoms 5 and 6 are in the $\{10\bar{1}1\}/\{0001\}$ edges and both have seven nearest neighbors, they are distinguishable by the arrangement of their neighbors. Atom 5 has five nearest neighbors on the surface (two neighbors buried inside the particle), while atom 6 has six nearest neighbors on the surface (only one neighbor buried inside the particle).

FIG 6. Cross-sectional views of the core-shell structure of Pt-Re nanoparticles simulated at T=600 K. Thes panels show (a) a [001] cross-section of the fcc cubo-octahedral $Pt_{75}Re_{25}$ nanoparticle (containing 586 atoms), and (b) a $[11\bar{2}0]$ cross-section of the hcp truncated bipyramidal $Pt_{25}Re_{75}$ nanoparticle (containing 587 atoms). The open circles represent the Pt atoms and the gray circles stand for the Re atoms.

FIG. 7. A series of snapshots of the fcc cubo-octahedral $Pt_{75}Re_{25}$ nanoparticle (containing 586 atoms) simulated at T=600 K. (a) the initial nanoparticle in which the Pt and Re atoms were distributed randomly at ideal fcc lattice positions; (b) after 5 million MC steps; (c) after 10 million MC steps; and (d) after 20 million MC steps. In these figures, the open circles represent the Pt atoms and the gray circles stand for the Re atoms. As a guide to the eye, one $\{100\}$ facet is delineated with dashed lines.

FIG. 8. Plot of the approximately linear relation between the atomic cohesive energy U/N (in eV) of fcc cubo-octahedral (circles) and hcp truncated hexagonal bipyramidal (squares) $Pt_{50}Re_{50}$ nanoparticles and $N^{-1/3}$ (the scaled number of atoms of these nanoparticles). The open circles and squares represent the results for nanoparticles in which Pt and Re atoms are distributed randomly, while the filled circles and squares are for nanoparticles in which Pt atoms segregate to surfaces.
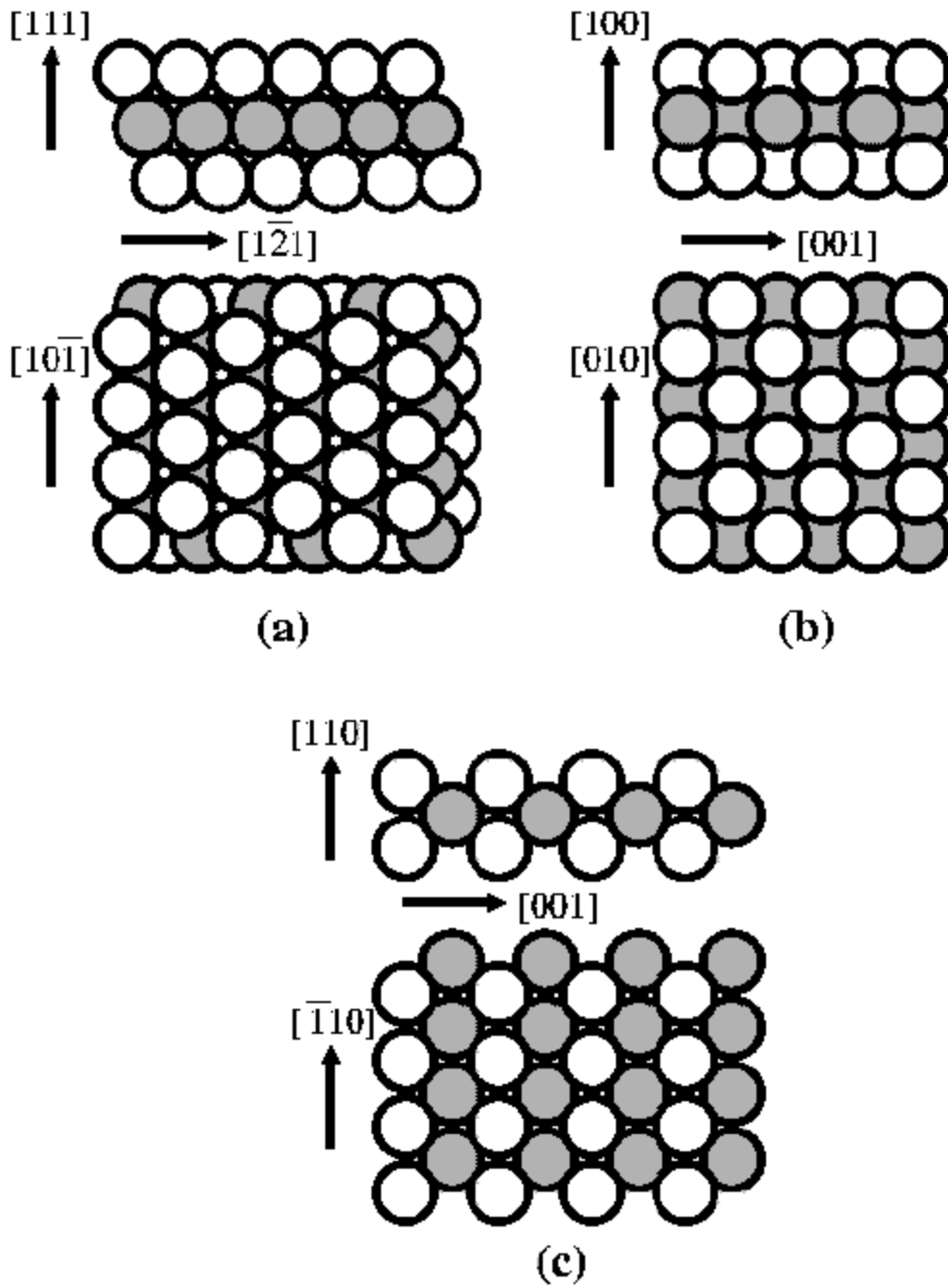
Figure 1, G. Wang et al

(a)

(b)

(c)

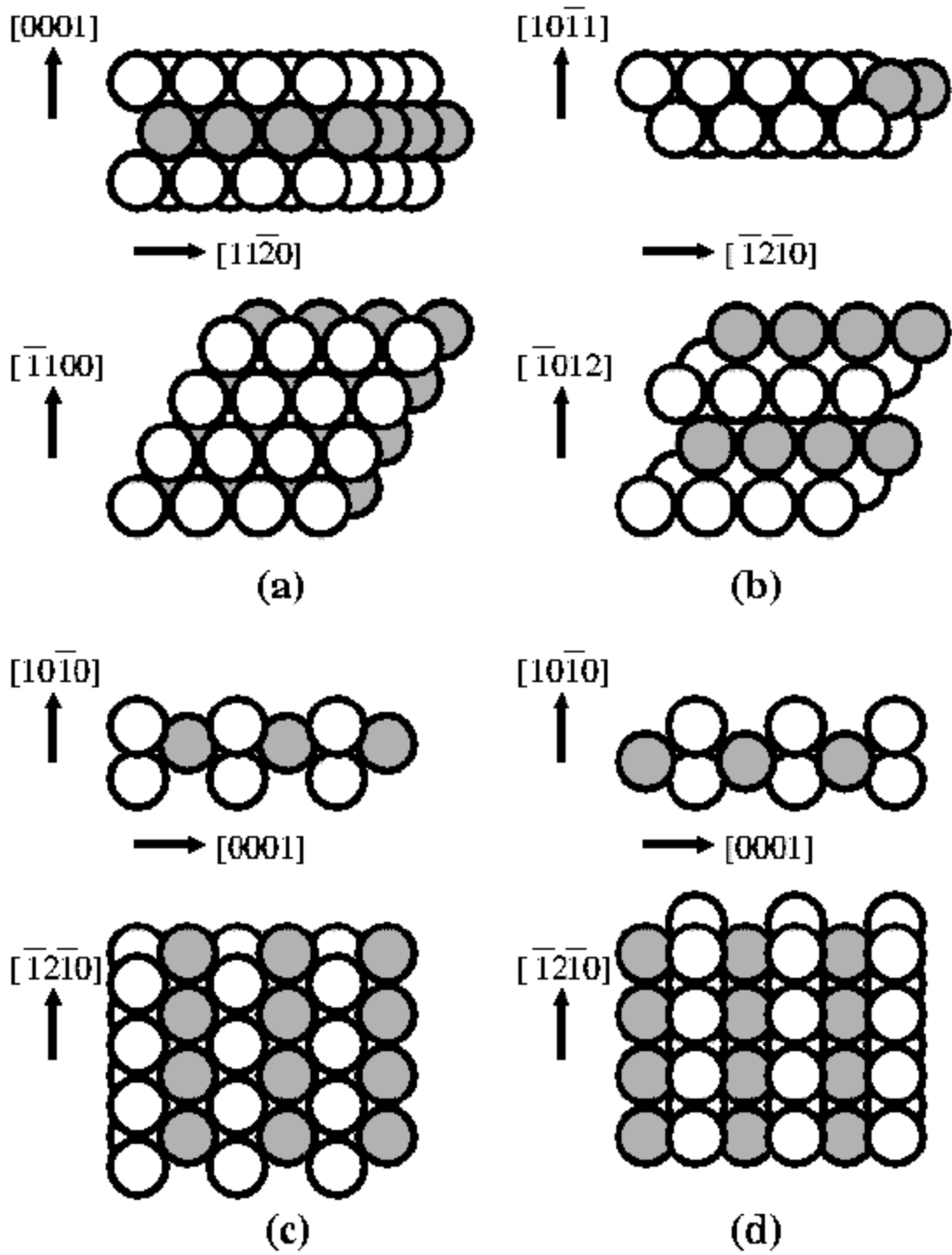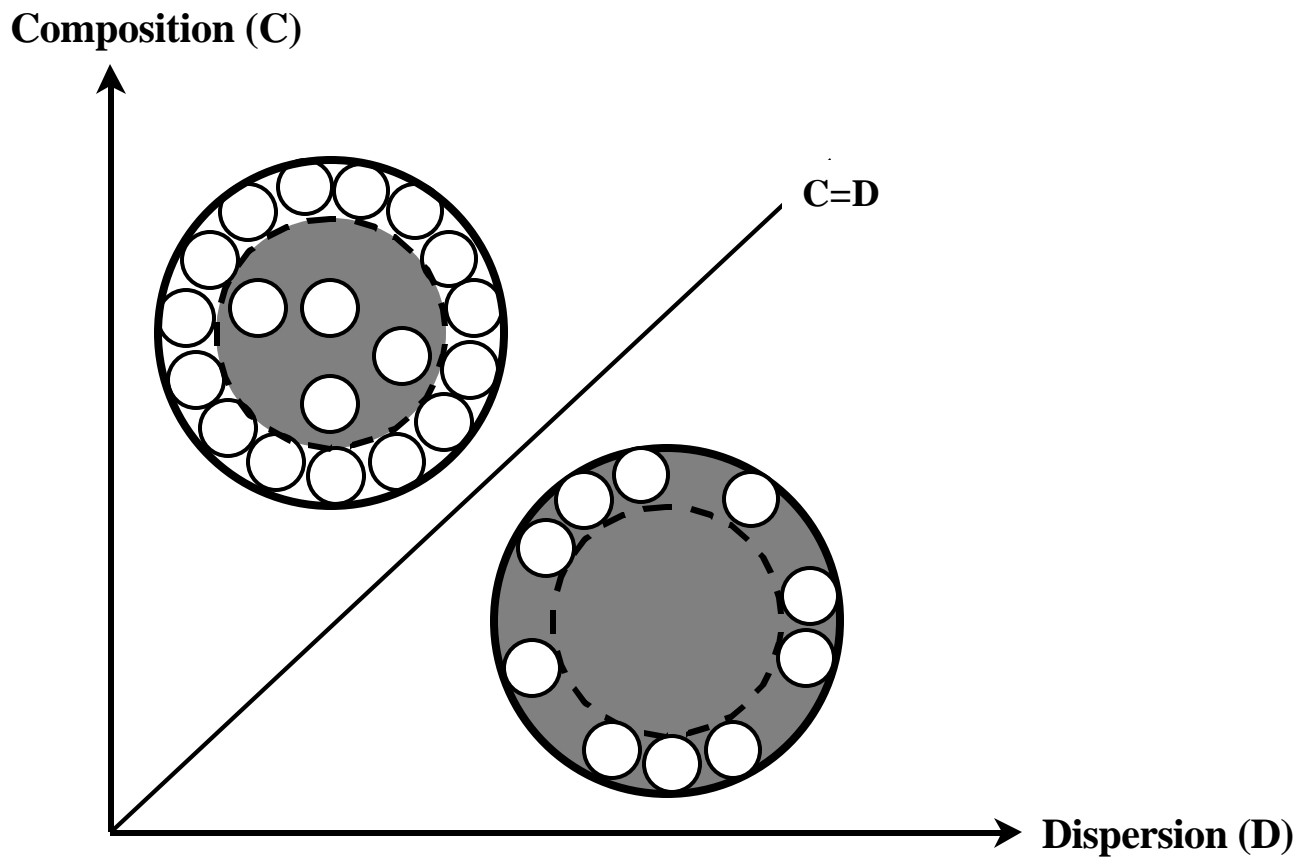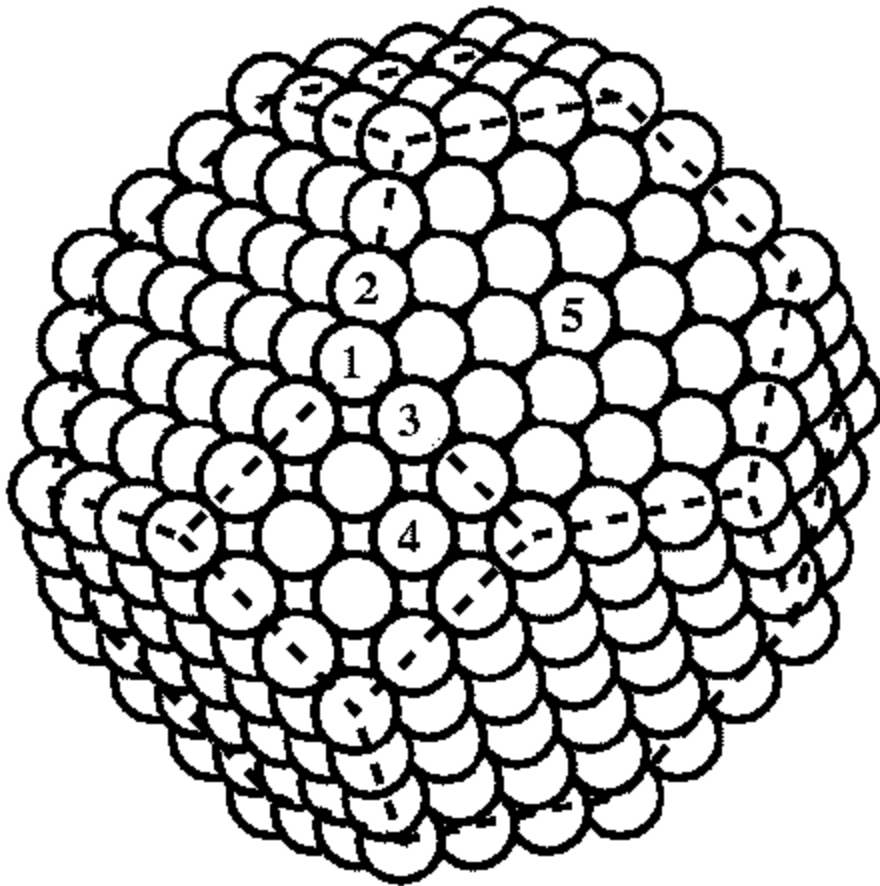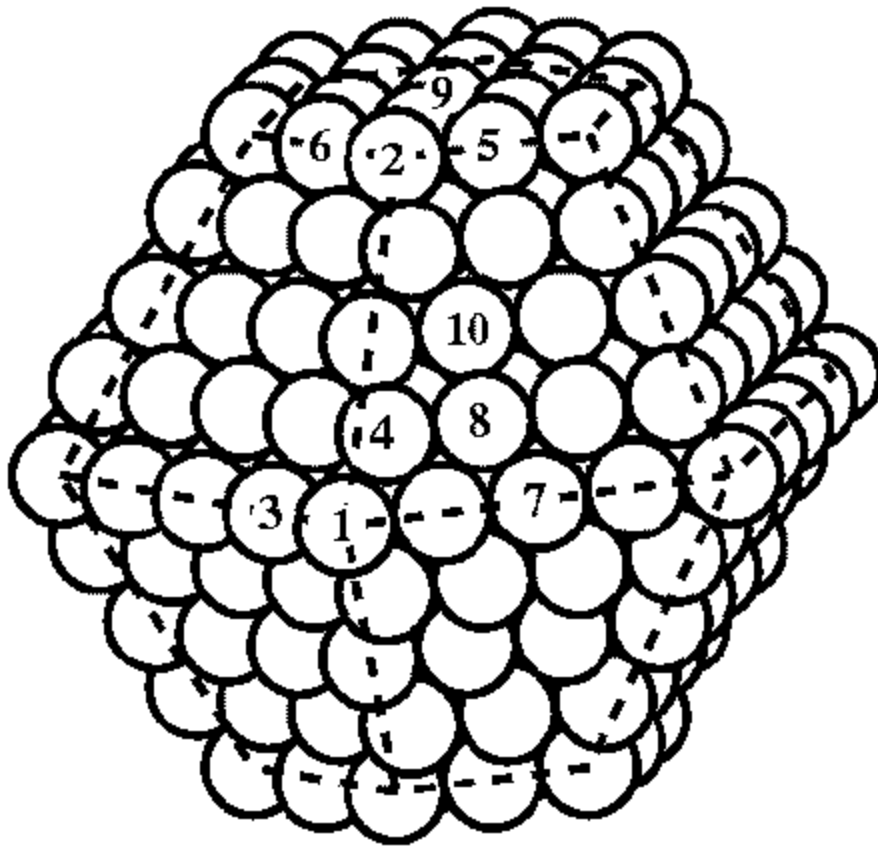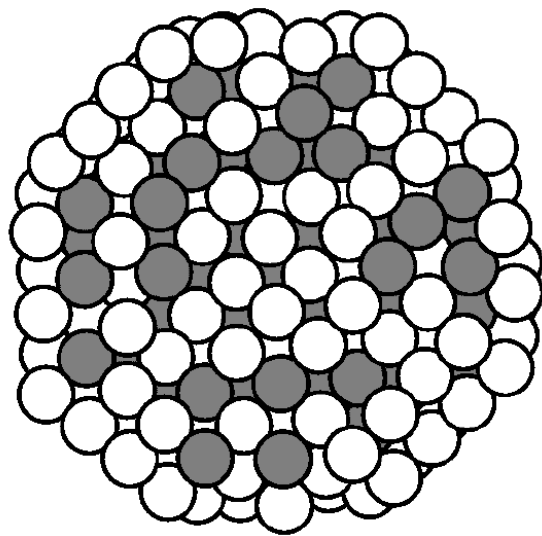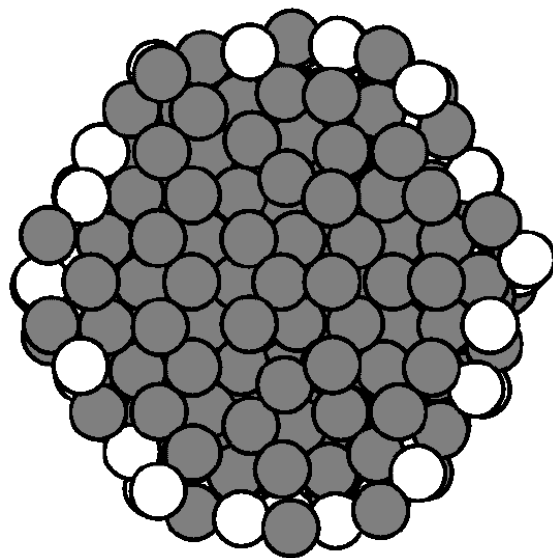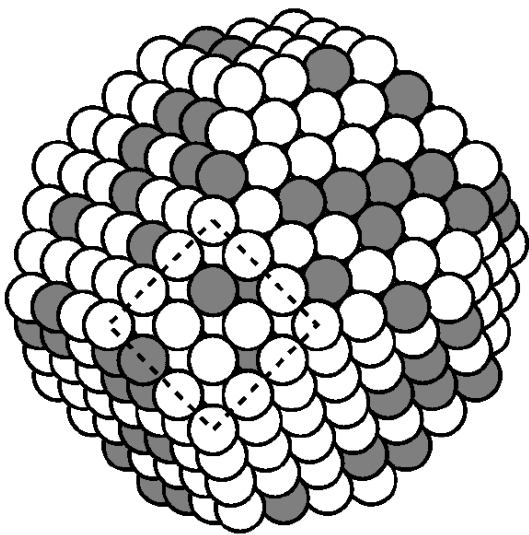(a)　　　(b)

(c)　　　(d)

Figure 3. G. Wang et al

Figure 5, G. Wang et al

(a)

(b)
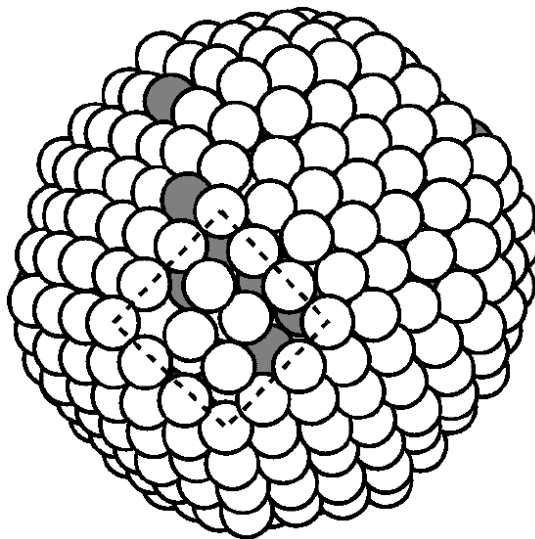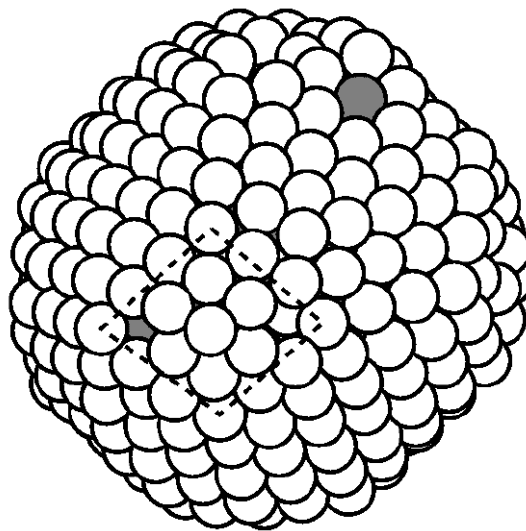
(a)

(b)
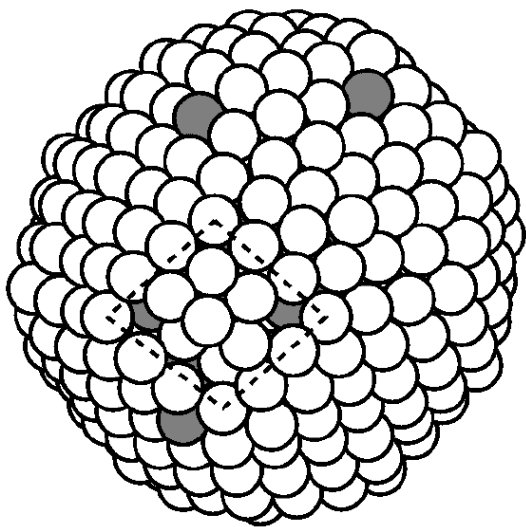
(c)

(d)

Figure 8, G. Wang et al

Fig 8. G. Wang et al